



Metal Oxide Supported Ni-Impregnated Bifunctional Catalysts for Controlling Char Formation and Maximizing Energy Recovery during Catalytic Hydrothermal Liquefaction of Food Waste

Journal:	<i>Sustainable Energy & Fuels</i>
Manuscript ID	SE-ART-11-2020-001662
Article Type:	Paper
Date Submitted by the Author:	08-Nov-2020
Complete List of Authors:	Cheng, Feng; Worcester Polytechnic Institute, Chemical Engineering Tompsett, Geoffrey; Worcester Polytechnic Institute, Chemical Engineering Fraga Alvarez, Daniela; Worcester Polytechnic Institute Romo, Carla; Worcester Polytechnic Institute Mckenna, Amy; Florida State University, National High Magnetic Field Laboratory Niles, Sydney; Florida State University, Department of Chemistry and Biochemistry Nelson, Robert; Woods Hole Oceanographic Institution, Marine Chemistry & Geochemistry; Reddy, Christopher; Woods hole Oceanographic Institution, Granados-Focil, Sergio; Clark University, Gustaf Carlson School of Chemistry and Biochemistry Paulsen, Alex; Mainstream Engineering Inc. Zhang, Ruihan; Worcester Polytechnic Institute Timko, Michael; Worcester Polytechnic Institute, Chemical Engineering

ARTICLE

Metal Oxide Supported Ni-Impregnated Bifunctional Catalysts for Controlling Char Formation and Maximizing Energy Recovery during Catalytic Hydrothermal Liquefaction of Food Waste†

Received 00th January 20xx,
Accepted 00th January 20xx

DOI: 10.1039/x0xx00000x

Feng Cheng¹, Geoffrey A. Tompsett¹, Daniela Valeska Fraga Alvarez¹, Carla I. Romo¹, Amy M. McKenna², Sydney F. Niles², Robert K. Nelson³, Christopher M. Reddy³, Sergio Granados-Fócil⁴, Alex D. Paulsen⁵, Ruihan Zhang⁶ and Michael T. Timko^{1,*}

Nickel (Ni)-impregnated metal oxide catalysts, Ni/CeZrO_x, Ni/ZrO₂, and Ni/CeO₂, were investigated to maximize energy recovery and reduce char yield during catalytic hydrothermal liquefaction (CHTL) of food waste. Yields of char, biocrude, water soluble products, and gas were measured at 300 °C and 1 hour for both the parent oxides (CeZrO_x, ZrO₂, and CeO₂) and the Ni-impregnated versions. Using Ni-based catalysts reduced the carbon-weighted char yield from 16-24% to <10% and decreased the energy recovery of char from 39-47% to <21%, as compared with control tests. In particular, using Ni/ZrO₂ resulted in the greatest biocrude yield, greatest reduction of char yield, and greatest energy recovered as biocrude (39.2%). After factoring in all forms of usable energy produced from food waste, the total energy recovery obtained for the catalysts studied here was >60%. Ni/ZrO₂ and Ni/CeO₂ show the greatest potential for controlling char growth and maximizing energy recovered from food waste. The crystalline structures of all three oxides were hydrothermally stable. Catalyst reuse tests indicate that the biocrude and char yields remained the same for the first and second use (within uncertainty) and that the catalyst retains its initial crystallinity and 93% of its initial Ni content. Molecular composition of biocrudes analyzed by the state-of-the-art analytical platforms (including GC-MS, GC×GC, FT-ICR MS, and ¹H NMR) revealed minor difference in the chemical constituents of biocrudes obtained using different catalysts that provide some insight regarding reaction mechanism.

Introduction

¹Department of Chemical Engineering, Worcester Polytechnic Institute, 100 Institute Rd., Worcester, MA 01609, USA.

²National High Magnetic Field Laboratory, Florida State University, 1800 E. Paul Dirac Dr., Tallahassee, Florida 32310-4005, USA.

³Department of Marine Chemistry and Geochemistry, Woods Hole Oceanographic Institution, 266 Woods Hole Rd., Massachusetts 02543, USA.

⁴Gustaf H. Carlson School of Chemistry and Biochemistry, Clark University; 950 Main Street, Worcester, Massachusetts 01610, USA.

⁵Mainstream Engineering Inc, 200 Yellow Place, Rockledge, FL 32955, USA.

⁶Department of Mechanical Engineering, Worcester Polytechnic Institute, Worcester, MA 01609, USA

* Corresponding Author. Tel. +1-508-831-4101; E-mail: mttimko@wpi.edu.

† Electronic Supplementary Information (ESI) available. See

DOI: 10.1039/x0xx00000x

Combustion of fossil fuels for transportation applications is the single largest source of greenhouse gas emissions, motivating development of renewable alternatives for decarbonizing the economy.¹ Biomass-derived fuels benefit from feedstock abundance and compatibility with existing distribution networks and combustion engines. Accordingly, first generation biofuels accounted for 5% of the total energy consumption in the U.S. in 2017,² with potential to increase to >20% with development of second generation biofuels.³

Despite its abundance, the cost of processing cellulosic biomass remains a bottleneck to economic production of second generation biofuels.³ Among potential alternative feedstocks, food waste generated from cafeterias, restaurants, food distribution centers, and food processing plants is particularly promising since its conversion to energy can offset petroleum usage while mitigating the

environmental impacts of landfill disposal.⁴ In the U.S. alone, approximately 77 million tons of food waste are produced annually, with more than 90% of it disposed of in landfills, leading to further emissions of the greenhouse-gas methane.^{5, 6} In addition, landfilled food-waste contaminates soil and groundwater during decomposition.^{4, 7, 8} For these reasons, many U.S. states have imposed tipping fees on food waste disposal.⁹

The main components of food waste are energy-rich carbohydrates, proteins, and lipids.¹⁰ Therefore, food waste has potential as a renewable feedstock that mitigates environmental problems associated with landfilling and offsets the use of petroleum-derived fuels for transportation, power, and heat.^{11, 12} Hydrothermal liquefaction (HTL) is a promising technique to convert wet food-waste into biofuels.¹³ Unlike pyrolysis, HTL does not require a dry feed, which benefits the overall energy balance for many feeds, including food waste.¹⁴ Compared with anaerobic digestion, HTL achieves rapid and efficient conversion of all feedstock components by thermal depolymerization under subcritical-water conditions.¹⁵ Accordingly, previous economic analysis indicates that HTL produces a fuel with a minimum selling price less than that of fuels produced from either pyrolysis or gasification¹⁶ and reduced greenhouse gas emissions compared with anaerobic digestion and pyrolysis.^{17, 18} The benefits are most apparent for lipid-rich feeds.¹⁹

HTL is normally performed at reaction temperatures between 180 and 374 °C, at pressures sufficient to maintain water in its liquid state (5–25 MPa), and with reaction times of between 5 and 120 minutes.²⁰ Under these conditions, water is in a subcritical state, acting as a solvent with intermediate to low polarity and with a tuneable self-ionization constant, thus generating H₃O⁺ and OH⁻ ions capable of catalyzing many reactions of interest.²⁰ Under these conditions, the main components of food waste can be converted into an energy-dense biocrude, via hydrolysis, Maillard reactions, decarboxylation, decarbonylation, aldol condensations, and other chemical transformations.^{15, 20, 21}

In addition to the biocrude product, HTL forms a char byproduct. Hydrochar produced under HTL conditions has some potential uses, such as a low-grade coal or as a precursor for activated carbon. However, char combustion efficiency is typically low due to its ash and volatile matter content.²² Use as an activated carbon requires extensive upgrading due to the presence of potentially toxic compounds and undesirable textural characteristics.²³⁻²⁵ Furthermore, char deposits can cause plugging and scaling problems in continuous flow systems, leading to downtime and potential safety issues.

Recently, catalytic HTL (CHTL) has been proposed as a method to increase biocrude yields.^{26, 27} Unfortunately, char produced in the presence of a heterogeneous catalyst forms a catalyst-char complex, further complicating catalyst use. Likewise, char deposits on catalyst surfaces potentially deactivate the catalyst by blocking access to its active sites.²⁸ These challenges drive the need to limit char formation during CHTL.

Char generation is difficult to control by reactor design alone under non-catalytic HTL conditions,²⁹ which motivates development of new approaches for controlling char selectivity and optimizing HTL product distribution. One potential approach is the use of homogeneous catalysts, such as Na₂CO₃ and KOH.^{30, 31} However, homogeneous catalysts are difficult to recover after reaction, resulting in potential environmental pollution. Reusable heterogeneous catalysts do not pose the same challenges as homogeneous versions making them a more attractive alternative.^{21, 27, 40} Noble metal catalysts have been reported to improve biocrude yield and reduce char yield,^{32, 33} but at great cost. Consequently, inexpensive, abundant catalyst materials are required to control char formation during CHTL while maintaining economic competitiveness.

Recent studies have found nickel to be an effective catalyst for char reduction under gasification conditions,³⁴ suggesting promise for adapting this approach to HTL reactions. Similarly, the use of Ni catalysts has been described for simultaneously promoting biomass gasification and tar reforming to produce H₂ under supercritical conditions.³⁵ Unlike noble metals, Ni is abundant and inexpensive, and Ni has been found to be stable and effective at char reduction in the presence of high-temperature water phases.^{36, 37} One potential concern is formation of Ni(CO)₄ under mild hydrothermal temperature (≤230 °C) in the presence of high pressure CO (27 MPa).³⁸ Ni(CO)₄ is a highly toxic gas and its formation contributes to catalyst deactivation. Fortunately, Ni(CO)₄ formation is not thermodynamically favored at temperatures >250 °C, meaning that operating at typical HTL conditions should avoid its formation. Since previous work on the use of Ni-based catalysts for char reduction has been performed at temperatures (over 800 °C) much greater than those typically used for HTL,³⁹ the implication of Ni catalysts at the lower temperatures associated with HTL remains a clear knowledge gap.

In this study, a series of metal oxide supported Ni catalysts were synthesized and evaluated for controlling char yields. ZrO₂, CeO₂, and CeZrO_x were studied as hydrothermally stable supports with potential catalytic functionality of their own.^{12, 40, 41} Food waste was used as the feed due to its potential as a negative cost feed in an HTL-based biorefinery. Catalyst effectiveness was examined by

measuring the yields of biocrude, char, and gas products obtained under standard conditions (300 °C reaction temperature and 1-hour reaction time). The results suggest new approaches for controlling char formation during HTL and maximizing energy recovered in usable products.

Methods

2.1 Food waste and catalyst materials

A standard feedstock of food waste was used for all experiments. The mixture consisted of American cheese, canned chicken, instant potatoes, green beans, white rice, apple source, and butter, in designated proportions (**Table 1**).⁴² The biochemical composition of food waste feedstock was estimated using the United States Department of Agriculture Food Composition data associated with the individual food items observed on the Nutrient Data Laboratory website.⁴³ Deionized water was added to prepare a food waste slurry with a solid content of 15 wt%, within the optimal range defined by previous studies.⁴⁴ The food waste slurry was stored in sealed jars at 4 °C prior to use. The particle sizes of the model food waste ranged from 11 to 100 μm, 75% of which were 21–60 μm, as described in the Supplementary Information (SI).

All chemicals used here were purchased from Sigma Aldrich with purities of >99.0%. Cerium and zirconium oxide (CeZrO_x) nanopowder, zirconium (IV) nitrate, cerium (III) nitrate, and nickel (II) nitrate hexahydrate were used for catalyst synthesis. Acetone was used for cleaning and biocrude extraction. Deionized water (electrical resistivity=18.0 MΩ·cm) was used for making food waste slurry for CHTL and HTL reactions. Nitrogen gas (purity>99.9%, Airgas) was used to pressurize the reactor prior to each run. Helium gas (grade 5.0, Airgas) was used for NH₃- and CO₂-temperature programmed desorption (TPD) analysis and as the gas chromatography carrier gas. CO₂ (grade 5.0, Airgas) and NH₃ (Middlesex gases anhydrous grade 99.995%) were used for titrating acid and base sites.

2.2 Preparation and characterization of catalyst

Oxide catalysts, ZrO₂ and CeO₂ were prepared by calcining their nitrate forms by heating under constant air flow (50 mL min⁻¹) at 5 °C min⁻¹ until reaching 500 °C, and then holding the final temperature for 3 h. Ni-based catalysts were prepared via the incipient wetness impregnation following the procedure reported by Liao et al.⁴⁵ Briefly, 15 g catalyst powder were wetted with Ni(NO₃)₂·6H₂O (1M) solution to obtain a mixture with 10 wt% nickel content. The precursor was dried overnight at a temperature of 120 °C and then calcined at 500 °C for another 3 h under air. The precipitated NiO was reduced at 350 °C for 3 h, in a tube furnace, at a hydrogen (H₂) flow

of 15 mL min⁻¹ to produce the Ni(10 wt.)/oxide catalyst.⁴⁵ Raman and XRD analysis of the synthesized catalyst confirmed successful Ni impregnation of the oxide supports (**Figure S1** in the SI).

Catalyst textural properties were evaluated using N₂ adsorption at -196.15 °C using a Quantachrome Autosorb iQ TPX instrument (Anton Paar Co., Graz, Austria). Before N₂ dosing, 500-1000 mg catalyst was degassed at 350 °C for up to 24 h under vacuum. Total surface area was estimated by fitting measured isotherms using the Brunauer–Emmett–Teller (BET) method. Mesopore diameters were estimated using Barrett, Joyner, and Halenda (BJH) method and the micropore volume and surface area using the Dubinin–Radushkevitch (DR) method.

The morphological characteristics and elemental distribution of the catalysts were determined using a scanning electron microscope (JSM 7000F SEM, JEOL Ltd., Tokyo, Japan) equipped with an energy-dispersive X-ray spectrometer.

The density of acid sites and base sites was quantified using NH₃- and CO₂-TPD, respectively. A Quantachrome Autosorb iQ adsorption/chemisorption system equipped with a thermal conductivity detector (TCD), was utilized for TPD analysis. The TPD methods recommended by Rodrigues et al., and Käßner et al.^{46, 47} were used. CO₂-TPD analysis involved first degassing the catalyst sample at 800 °C under 20 mL min⁻¹ helium flow for 240 minutes, followed by cooling to 30 °C. Afterwards, the degassed catalyst sample was saturated under CO₂ flow for 10 min. The sample was then purged with helium gas for 30 min at 30 °C to eliminate free CO₂. Finally, the CO₂-saturated catalyst was heated to 800 °C at a heating rate of 10 °C min⁻¹ under helium atmosphere. The off-gassed CO₂ was quantified using a calibrated TCD detector.

A similar method was used for NH₃-TPD analysis, following the procedure recommended by Käßner et al.⁴⁶ Catalyst was heated to 800 °C (10 °C min⁻¹), allowed to degas for 120 min, and then cooled to 100 °C. NH₃ was introduced to the sample to saturate it for 10 minutes. The NH₃-saturated catalyst was flushed with helium gas for 30 min, then heated at 2 °C min⁻¹ from 100 to 800 °C. Off-gassed NH₃ was again quantified using the TCD detector.

The TCD detector used for quantifying both acid and base sites was calibrated by injection of known volumes of NH₃ or CO₂ into the chemisorption cell under constant helium flow. The area under the TPD response curve was integrated using Magicplot software.

The crystalline structures of the oxide catalysts with and without nickel doping were characterized by X-ray

diffraction (XRD) before and after use. A Rigaku automatic instrument (Geigerflex, Rigaku Co., Tokyo, Japan) in the Bragg-Bretano theta-theta configuration was used for XRD analysis. All measurements were performed using CuK α radiation (1.5406 Å wavelength) at 27.5 kV and 25 mA, scanning over the 2 θ angle range from 6° to 80° at a rate of 0.02° s⁻¹. XRD patterns were baseline and background corrected using Jade 6 software. Peaks were fitted to Lorentzian shapes to determine peak position and full-width half maximum (FWHM) using MagicPlot. The size of nickel particles on the oxide supports was estimated by the Scherrer equation, using K=0.9 to estimate the shape factor.

The oxide phases present in the solid oxide catalysts were studied using Raman spectroscopy (Xplora, Horiba Scientific, Piscataway, NJ, USA). All samples were analyzed using an excitation laser at 532 nm and an Olympus 100 \times magnification lens. The resulting laser power was maintained in the 1–5 mW range. The acquisition time was 2 s with 10 scans, acquired for each sample; average spectra are presented here. The spectra from multiple particles of the transition metal oxides were acquired to evaluate heterogeneity.

The nickel loadings of catalysts before and after CHTL were determined using an inductively coupled plasma mass spectrometer (ICP-MS) (Nexion 350x, PerkinElmer Co., Waltham, MA).

Catalysts were characterized as synthesized, after use for reaction, and after separate endurance tests consisting of placing the catalyst in the HTL reactor at 300 °C and 20.68 MPa for 16 h.

2.3 Hydrothermal liquefaction of food waste

CHTL reactions were conducted in a 300-mL stainless-steel bench-top batch reactor (Model 4841, Parr Instrument Co., Moline, IL, USA) with a rated maximum temperature of 350 °C and a maximum pressure of 24.1 MPa. The batch reactor was equipped with a gas entrainment impeller (maintained at 600 rpm throughout the reaction) and an external heating jacket.

For each reaction test, 100 g of feedstock containing 15 g of dry food waste and 85 g of water was loaded into the batch reactor. When catalyst was used in the test, either 5 g of the oxide catalyst or 5.5 g Ni-impregnated oxide were loaded along with the slurry. Differing amounts of oxide and Ni-impregnated oxide material were used so that the amount of oxide was consistently 5 g, with approximately 0.5 g of Ni loaded when Ni-impregnated catalysts were tested. The loaded reactor was weighed to determine its total mass with ± 1.0 g precision. After weighing, the reactor was sealed, purged using nitrogen to remove air, pressurized with 2.1 MPa of hydrogen (H₂) in runs where it

Table 1. Components in the food waste feedstock and corresponding composition and higher heating value data.

Food Item	Feedstock Percent (wt%, d.b.)	Feedstock Composition and HHV	Value
American Cheese	12.8	Moisture (wt%, w.b.)	73.0
Canned Chicken	14.9	Protein (wt%, d.b.)	17.8
Instant Potatoes	10.6	Lipid (wt%, d.b.)	21.9
Green Beans	14.9	Carbohydrate (wt%, d.b.)	58.9
White Rice	19.1	Ash (wt%, d.b.)	1.1
Apple Sauce	22.3	HHV (MJ kg ⁻¹ , d.b.)	24.6
Butter	5.4	HHV (MJ kg ⁻¹ , w.b.)	6.5

HHV: Higher heating value. d.b.: Dry basis. w.b.: Wet basis.

was used, and finally pressurized to 7.6 MPa using nitrogen (N₂). An additional control experiment was conducted in the absence of catalyst in pure N₂ atmosphere. Following previous work,^{12, 48} reaction conditions were selected as 300 °C and 1 h. These conditions represent a balance between energy use, biocrude yield, and biocrude heteroatom content.⁴⁹ The reactor was heated to 300 °C at a heating rate of 6 °C min⁻¹ and maintained at 300 \pm 3 °C for 1 h. The pressure was \sim 20.6 MPa when the reaction temperature was reached, sufficient to maintain water in its liquid state.⁵⁰

Upon completion of the CHTL reaction, the reactor vessel was quenched by lowering the temperature to 40 °C within 10 min by immersion in an ice-water bath. The reactor was weighed to compare with the initial weight to check for leaks that may have occurred during the run; only experiments in which the initial and final reactor mass agreed to within measurement uncertainty (± 1.0 g) are reported here. Headspace gas generated during the reaction was collected with a Restek 3 L gas bag, using a two-value system. The gas bag was sealed and transferred to the GC. The reaction gas composition was measured using a GC sample-loop. The weight of gas was determined from the difference between the masses of the full and deflated gas bag.

All CHTL and HTL runs were conducted in duplicate or triplicate with the measured product yields consistent to within $\pm 5\%$. Average values are reported here and uncertainties are estimated from the standard deviation obtained from replicate experiments.

Following quenching and depressurizing, the HTL product mixture was transferred from the reaction vessel, and vacuum filtered (125 mm diameter, 11 μ m pore size filter paper) separate the aqueous phase from the solid and

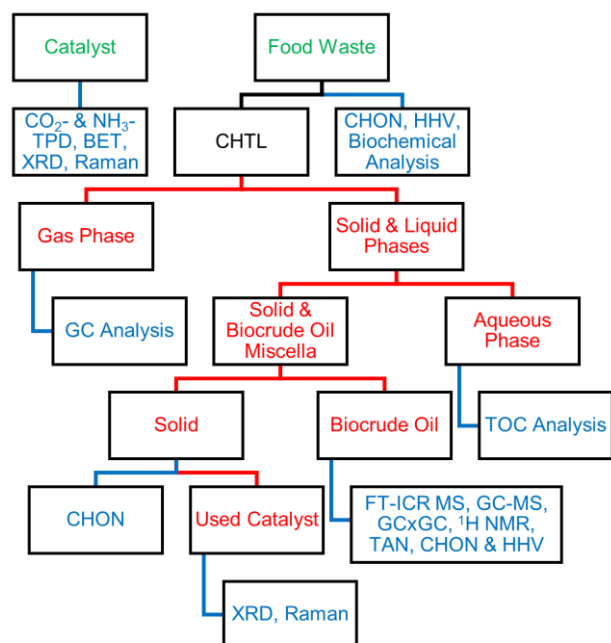


Figure 1. Schematic diagram of CHTL experimental procedure and characterization methods. Green words/lines represent feedstock. Red words/lines represent HTL product. Blue words/lines represent analytic methods. TPD: temperature programmed desorption. BET: Brunauer–Emmett–Teller method. XRD: X-ray powder diffraction. CHTL: catalytic hydrothermal liquefaction. HHV: higher heating value. GC: gas chromatography. TOC: total organic carbon analysis. CHON: elemental analysis. FT-ICR MS: Fourier transform ion cyclotron resonance mass spectrometry. GC-MS: gas chromatography followed by-mass spectrometry. GCxGC: two-dimensional gas chromatography. $^1\text{H NMR}$: proton nuclear magnetic resonance. TAN: total acid number.

biocrude phases. The filter cake consisted of catalyst, char, and biocrude. It was rinsed with excess acetone to separate the biocrude from the solids. Biocrude was collected by acetone stripping with a rotary evaporator at 54 °C under vacuum atmosphere. The aqueous and biocrude phases were sealed and stored at 4 °C for characterization.

The solid remaining after acetone extraction consisted of char and used catalyst. It was dried at 60 °C overnight,

weighed, and stored in a desiccator for future analysis. Char was removed from the used catalyst by placing the HTL solids in a quartz tube furnace at 550 °C for 3 h under air flow (50 mL min⁻¹). The char yield was determined as the difference between the weight of the solids before and after the thermal treatment. The used catalysts were regenerated using air combustion and sequential H₂ reduction at the same conditions that were used to prepare fresh catalyst (Section 2.2).

2.4 Characterization of HTL products

Figure 1 is a schematic representation of the feedstock and HTL product characterization methods. The elemental (CHON) contents of dried feedstock, HTL solids (including catalyst), and biocrude were characterized using an elemental analyzer (Midwest Micro Lab, Indianapolis, IN, USA).

The higher heating value (HHV) of the dried solid samples (containing char and catalyst) was estimated using the Demirbas equation,⁵¹ reported previously. In addition, the experimental HHV values of dried feedstock and biocrude were obtained using a semi-micro calorimeter (25720, Parr, Moline, IL, USA). The instrument was calibrated using benzoic acid as a standard.

Biocrude composition was analyzed using gas chromatography followed by-mass spectrometry (GC-MS), positive-ion (+) atmospheric pressure photoionization Fourier transform ion cyclotron resonance mass spectrometry (APPI FT-ICR MS),^{52, 53} proton nuclear magnetic resonance ($^1\text{H NMR}$) spectroscopy, comprehensive two-dimensional gas chromatography (GCxGC), and total acid number (TAN). Details of sample preparation and operation procedures are provided in the SI.

Table 2. Surface areas, base and acid site densities of solid catalyst materials.

Catalyst	BET surface area ^a (m ² g ⁻¹)	BJH mesopore diameter ^b (nm)	DR micropore volume ^c (cm ³ g ⁻¹) and surface area (m ² g ⁻¹)	Base site density from CO ₂ -TPD (μmol m ⁻²)	Acid site density from NH ₃ -TPD (μmol m ⁻²)
CeZrO _x	45	4.8	0.015, 41	0.332	0.006
ZrO ₂	84	9	0.028, 78	0.276	0.007
CeO ₂	64	17	0.026, 74	0.279	0.012
Catalyst	BET surface area ^a (m ² g ⁻¹)	BJH mesopore diameter ^b (nm)	DR micropore volume ^c (cm ³ g ⁻¹) and surface area (m ² g ⁻¹)	Nickel loading in catalyst (wt%)	Ni particle diameter ^d (nm)
Ni/CeZrO _x	38	2.5	0.013, 35	8.9 ± 0.2	25.9
Ni/ZrO ₂	52	4.8	0.019, 53	8.2 ± 0.2	25.3
Ni/CeO ₂	67	8.6	0.023, 64	9.2 ± 0.4	25.8

^a BET: Brunauer–Emmett–Teller analysis; ^b BJH: Barrett, Joyner, and Halenda method; ^c DR: Dubinin-Radushkevitch method, more accurate for microporous materials. ^d Estimated by Scherrer Equation. Ranges represent the standard deviation of three repeated tests.

Table 3. The elemental composition, higher heating value (HHV), and energy recovery (ER) of biocrude oil.

	C (wt%)	H (wt%)	N (wt%)	O ^a (wt%)	HHV (MJ kg ⁻¹)	ER _{biocrude oil} (%)	ER _{biocrude oil} (%) (H ₂ co-feed included)	ER _{biocrude oil} Improvement (H ₂ co-feed included) ^b
Food Waste	47.2	6.7	4.6	41.5	24.6			
HTL (H₂)	67.7±3.8	8.9±0.4	4.2±0.7	19.3±3.9	36.1±1.6	34.0±5.1	30.8±4.6	1.13
CeO₂	73.7±0.4	8.8±0.1	4.4±0.1	13.1±0.4	38.9±1.9	34.5±1.9	31.2±1.7	1.15
ZrO₂	71.8±1.6	9.2±0.3	3.8±0.2	15.3±1.7	37.7±1.4	33.4±1.8	30.3±1.6	1.11
CeZrO_x	71.7±1.5	8.7±0.2	3.8±0.7	15.8±1.7	37.6±1.3	37.6±2.8	34.1±2.6	1.25
Ni/CeO₂	66.7±6.8	8.1±0.8	4.3±0.7	20.9±6.9	34.6±3.7	35.6±3.8	32.3±3.5	1.19
Ni/ZrO₂	72.9±3.0	9.3±0.8	5.5±2.1	12.3±3.8	39.3±0.8	43.2±1.6	39.2±1.5	1.44
Ni/CeZrO_x	68.3±7.7	8.3±0.7	4.5±0.1	18.6±7.8	37.3±0.1	35.5±6.0	32.2±5.5	1.19

^a By difference. ^b ER Improvement is equal to the ratio of ER (catalysts and H₂) to ER of control (neither catalyst nor H₂). Ranges represent the standard deviation of either two or three repeated tests.

The organic carbon content of the CHTL aqueous fractions was determined using a total organic carbon (TOC) analyzer (Shimadzu Co., Kyoto, Japan) and all measurements were conducted in at least duplicate.

The gaseous products were analyzed by GC (GC-2014, Shimadzu Co., Kyoto, Japan) equipped with a TCD and an 80/100 Hayesep Q packed column (3 m × 0.125 in × 2.1 mm SS). Samples were injected into the inlet using a 102 µL sample loop via an automated valve. The temperature program consisted of an initial temperature of 30 °C, followed by heating to 90 °C (5 °C min⁻¹), holding for 20 min, then heating to 130 °C (5 °C min⁻¹), and finally heating to 150 °C (10 °C min⁻¹). The final temperature was held at 150 °C for 40 min until all products had eluted. The peak areas of gaseous compounds were integrated and identified using retention time matching with known standards. TCD response was quantified using known standards.

The carbon yields of char, biocrude, aqueous phase, and gases were determined using the following equation:

$$\text{Carbon Yield}_{\text{product}} = \frac{\text{Mass}_{\text{product}} \times \text{Carbon \%}_{\text{product}}}{\text{Mass}_{\text{feedstock}} \times \text{Carbon \%}_{\text{feedstock}}} \times 100\%$$

which utilizes the measured product masses and carbon weight fractions. The carbon content of the biocrude was estimated based on elemental analysis. The carbon content of the gas product was estimated based on the measured compositions of CO₂, CO, CH₄, and C₂H₄ in the gas phase. The carbon content of aqueous phase was estimated by measuring the TOC of aqueous phase.

Carbon yields in the biocrude, char, aqueous phase, and gas products were summed to check for closure of the overall carbon balance. In most cases, the carbon balance closed to within 5%, while only in the case of Ni/CeZrO_x, the carbon balance closed to within 5-20%, due to residual

char and biocrude that could not be physically recovered from the reactor. For the control test, i.e. non-catalytic HTL in the presence of H₂, the carbon balance exceeded 100%, but the excess was well within measurement uncertainty. In the interest of transparency, carbon yields are reported without normalization to account for losses.

The energy recovery (ER) in a given product was defined as a ratio of the energy stored in that product relative to the combined energy stored in the food waste and H₂ charged to the reactor:

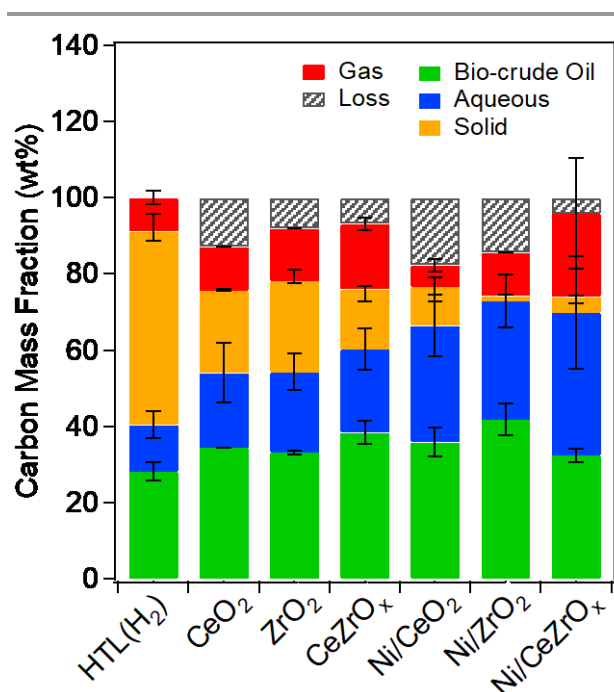


Figure 2. Carbon distribution among different HTL products without/with using hydrogen and catalysts. The operating condition was 300 °C and 60 min. HTL(H₂): Thermal run (with H₂ no catalyst). Error bars represent the range or standard deviation of either two or three repeated tests.

$$ER = \frac{\text{Mass}_{\text{product}} \times \text{HHV}_{\text{product}}}{\text{Mass}_{\text{dry feed}} \times \text{HHV}_{\text{dry feed}} + \text{Mass}_{\text{H}_2} \times \text{HHV}_{\text{H}_2}} \times 100\%$$

where HHV denotes higher heating value and subscripts are used to specify the product category.

Results and Discussion

The purpose of this study was to evaluate the catalytic performance of Ni-based catalysts for HTL of food waste, with specific emphasis on char reduction and energy recovered as usable products. This work comprises four components: 1) characterization of catalysts, 2) test of catalytic performance, 3) stability of catalysts, and 4) molecular characterization of the biocrude product to gain insight into reaction pathways.

3.1 Characterization of Ni-Impregnated Oxides

ZrO₂, CeO₂, and CeZrO_x were impregnated with Ni to confer catalytic HTL activity to reduce char formation while maintaining biocrude yield. Synthesis techniques – described in the Methods Section – were selected to produce mesoporous oxides, primarily consisting of base sites, and possessing consistent Ni loading as uniformly distributed metallic nanoparticles. Accordingly, the synthesized catalysts were characterized using N₂ sorption to evaluate textural properties, NH₃- and CO₂-TPD to

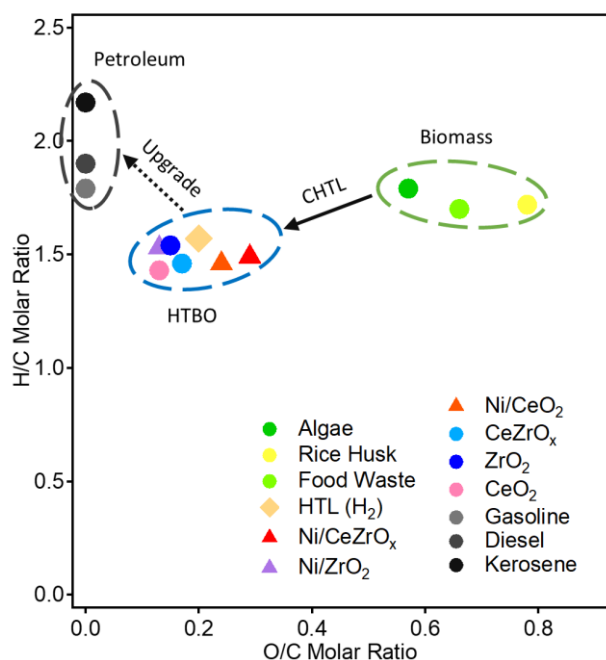


Figure 3. The van Krevelen plot of H/C vs. O/C molar ratio for different feedstocks, HTL biocrude oil, and different types of crude oil products. The CHTL operating condition are 300 °C, 20.7 MPa for 60 min. H/C and O/C error bars are within +/- 0.2 and +/- 0.1, respectively.

quantify base and acid sites densities (**Figures S2 and S3**), XRD to identify crystal phases and estimate Ni nanoparticle sizes, acid digestion followed by ICP-MS analysis to quantify Ni content, and SEM to evaluate particle morphology. **Table 2** summarizes the results obtained for the metal oxide supports and the corresponding Ni-impregnated metal oxides. Raw data, including XRD diffractograms and SEM images, are provided in **Figures S1 and S4**.

Table 2 shows that the Ni-impregnated catalysts have surface areas greater than 40 m² g⁻¹, consistent with porous structures.⁵⁴ Ni impregnation decreases surface area and micropore volume of parent oxides by <40%. BJH estimates of pore diameters range from 2 to 17 nm all catalysts.⁵⁵ In all cases, these pore diameters are sufficient to provide access to small molecules obtained by hydrolysis of lipids, polypeptides, or oligosaccharides initially present in the feed.^{56, 57}

Figure S4 provides SEM images and EDS composition maps of the synthesized Ni-based catalysts. Ni/CeO₂ exhibits a brick-like structure with smaller irregular particles embedded on the catalyst surface. Ni/ZrO₂ exhibits an angular flaky structure with irregular texture. Ni/CeZrO_x forms aggregates, with each aggregate consisting of thousands of nanoscale particles. Measured nickel particle sizes were similar on all catalysts (approximately 26 nm, see **Table 2**). EDS maps of the oxide surfaces indicate uniform nickel nanoparticle distribution (**Figure S4**). ICP-MS analysis of acid digested catalysts indicated consistent nickel loading between 8.2 and 9.2 wt% (**Table 2**).

Figure S1 provides XRD diffractograms of the synthesized catalysts. Based on comparison with crystallography databases, ZrO₂ was found to be a mixture of its monoclinic (JCPDS-ICDD #37-1484) and tetragonal phases (JCPDS-ICDD #50-1089).⁵⁸ CeO₂ was synthesized as its cubic fluorite phase (JCPDS-ICDD #81-0792).⁵⁹ CeZrO_x forms a complex crystal structure (JCPDS-ICDD #38-1436) that is consistent with observations made in previous studies.⁶⁰ After impregnation, Ni is present in its metallic state, as indicated by the appearance of its characteristic peak at 44.6° (JCPDS-ICDD #87-0712).⁶¹

Raman spectra (**Figures S5-S7**) are consistent with XRD patterns and literature. More detail is provided in the SI and the most important conclusion that can be drawn from the Raman spectra is that minimal Ni inclusion occurs in the oxide crystal structures themselves.

NH₃- and CO₂-TPD indicate that all three supports were primarily basic, as summarized in **Table 2**. Cheng et al. previously reported optimal biocrude yields for mixed metal oxides with approximately 50-150 times more base sites than acid sites, irrespective of strength.⁴⁸ The three catalysts studied here fall at the edge of this range, with base-to-acid site

densities ranging narrowly from 23 to 55. The acid/base content of the Ni-impregnated catalysts could not be measured due to partial oxidation of Ni particles during TPD analysis.⁶² Because the metal content is <10 wt%, the effect of nickel loading on the bulk acid-base properties of the underlying oxides is not expected to change after nickel impregnation.⁶³

In summary, the Ni-impregnated catalysts exhibit similar textural properties, metal loading, and acid-base properties to one another, facilitating direct comparison of catalytic performance. Moreover, all of these properties fall within the ranges previously identified as appropriate or optimal for HTL conversion of the proteins, carbohydrates, and lipids present in food waste.⁴⁸

3.2 Evaluation of Catalyst Performance for HTL of Food Waste

The performance of Ni/CeO₂, Ni/ZrO₂, Ni/CeZrO_x, and their parent oxides was investigated for CHTL of food waste with emphasis on char inhibition and biocrude yield. Non-catalytic HTL reactions were performed as controls at the same conditions as the CHTL experiments – i.e., at the same temperature, reaction time, and hydrogen loading. In addition, data were collected for non-catalytic HTL in the absence of H₂. These data are provided in the SI. In all experiments, the composition and higher heating values of biocrude, gas, and char were measured or estimated to complete the energy balance and determine the energy recovered in the main product phases. **Figures 2-5** and **Tables 3-6 and S1** summarize these results.

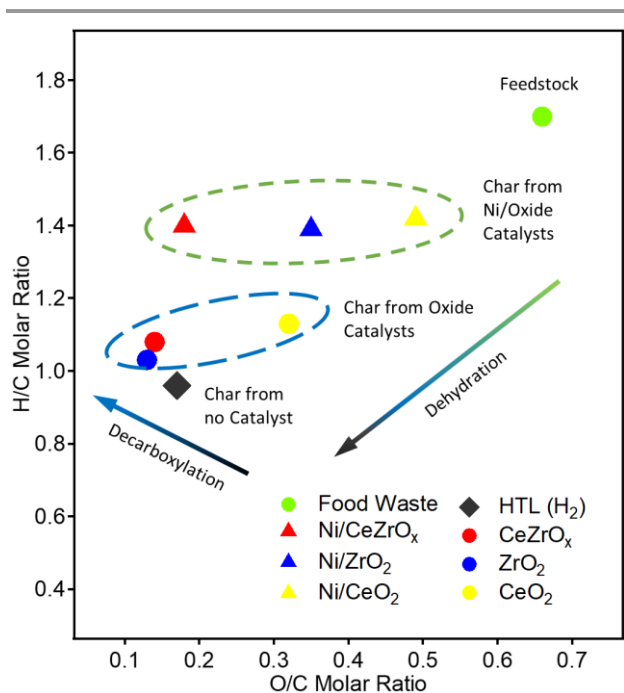


Figure 4. The van Krevelen plot of H/C vs. O/C molar ratio for HTL char. The CHTL operating condition are 300 °C, 20.7 MPa for 60 min. H/C and O/C error bars are within +/- 0.2 and +/- 0.1, respectively.

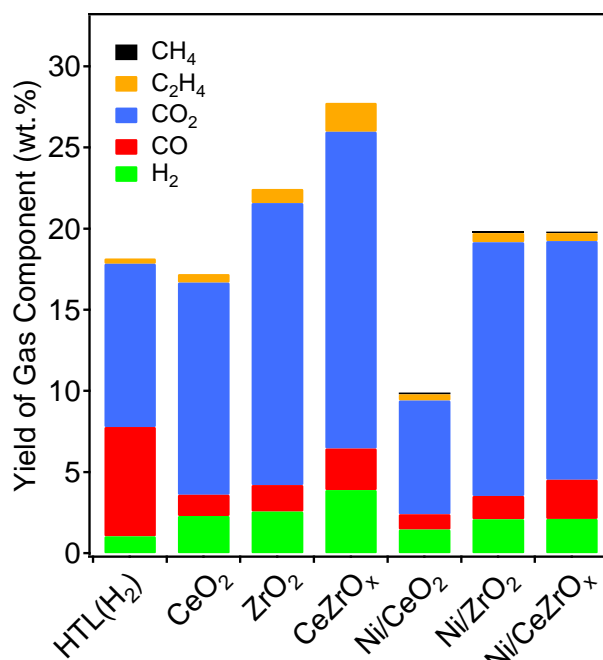


Figure 5. The yields of gas components from HTL of food waste without and with different catalysts. The operating conditions were 300 °C, 20±0.5 MPa H₂, and 60 min. HTL(H₂): Thermal run (with H₂ no catalyst).

Figure 2 and **Table S2** provide carbon yields as biocrude, gas, aqueous phase, and char products. Use of metal oxides reduced char yield relative to those obtained without catalyst, with the greatest benefit observed for CeZrO_x. The superior performance of CeZrO_x relative to other oxides is consistent with its possessing a base-to-acid density ratio closer to the optimal range as previously identified.⁴⁸ In addition, ceria containing materials possess oxygen vacancies that can play a catalytic role, especially for reduction of oxygen bearing compounds under reducing environment.⁶⁴ These results are consistent with the use of metal oxides for directing HTL pathways away from char.^{12, 48}

Figure 2 shows that use of the Ni-impregnated oxide catalysts resulted in further incremental increase in biocrude carbon yield, with the improvement greater than experimental uncertainty for Ni/ZrO₂, but not for Ni/CeO₂ or Ni/CeZrO_x. The real benefit of the Ni-impregnated catalysts, much greater than uncertainty, is reduction of char. Here, the carbon yield obtained as char decreased from 50% for non-catalytic HTL, to 15-24% for the oxide catalysts, to <10% for the Ni-impregnated catalysts. Use of Ni/ZrO₂ resulted in nearly immeasurable char carbon yields (1.3%).

Concomitantly with char reductions, use of the Ni-impregnated oxides promoted formation of water-soluble carbon that appeared as aqueous-phase products. The carbon yield in the aqueous phase increased from 12% for

non-catalytic HTL (H_2) to approximately 37% for the Ni-impregnated oxide catalysts. Promoting pathways that form water soluble carbon instead of char can be beneficial for catalyst lifetime.⁶⁵ Moreover, the water soluble carbon produced during HTL is appropriate for hydrothermal gasification or anaerobic digestion to produce renewable natural gas (RNG). Accordingly, reducing char yields without sacrificing biocrude yields and increasing yields of water-soluble carbon products can increase the overall value of the HTL products.

Decreasing char yields cannot come at the detriment of biocrude composition. **Tables 3 and S2** provide CHON elemental analysis for the biocrudes shown in **Figure 2**. As expected, non-catalytic HTL increases the carbon content of the feed from 47.2 wt% to 67.7 wt%, with a corresponding decrease in oxygen content. Interestingly, use of all catalysts evaluated here results in biocrudes with similar carbon and oxygen content compared with that observed under non-catalytic HTL conditions. Therefore, the char reduction shown in **Figure 2** does not sacrifice biocrude composition.

The compositional changes between samples are rapidly visualized with plots of H/C vs O/C ratios for detected compounds in van Krevelen diagrams.⁶⁶ **Figure 3** shows the van Krevelen plot corresponding to the biocrude products shown in **Figure 2** and **Table 3**. Data points for several important feedstocks and hydrocarbon fuels are annotated for reference.⁶⁷⁻⁷⁰ As expected, CHTL reduces O/C ratios, from approximately 0.7 to 0.25-0.35 depending on the catalyst. Uncertainties in O/C and H/C are sufficient that all but the most separated biocrudes are roughly equivalent, meaning that composition is only weakly dependent on catalyst. Similarly, and again independent of catalyst, the H/C ratio of the biocrude is approximately 1.5. The H/C ratio of petroleum-derived fuels is ~ 1.8 , indicating the need for biocrude hydrotreating,^{69, 70} shown by the dotted arrow in **Figure 3**. The nitrogen content data showed in **Table 3** indicates that hydrotreating the biocrude must reduce its nitrogen content in addition to removing oxygen.

Table 3 provides HHV data measured for the biocrude. In all cases, the HHVs of the biocrudes were significantly greater than the original food waste, approximately 36 MJ kg^{-1} compared with 24.6 MJ kg^{-1} . HHVs measured for the different conditions were tightly clustered around 36 MJ kg^{-1} , with the biocrude obtained using Ni/ZrO₂ as the only statistical outlier with an HHV of 39.3 ± 0.8 MJ kg^{-1} .

Similarly, the total acid number (TAN) of the biocrudes was measured, as shown in **Table S3**. TAN was >100 mg KOH g^{-1} for most of the catalysts used here, indicating that the biocrude will need to be upgraded prior to its use as a transportation fuel.

Figure 4 shows the van Krevelen plot of the char products. Thermal conditions produce a char with an H/C ratio less than any of the other samples. Similarly, the O/C ratio of the thermal char is among the least of those studied here. The H/C ratio of chars produced in the presence of metal oxides are slightly greater than that observed for the thermal char. Interestingly, the O/C ratio of the char formed in the presence of CeO₂ was significantly greater than that formed in the presence of ZrO₂ or CeZrO_x. Finally, H/C ratios of the chars formed in the presence of Ni-impregnated oxides were roughly uniform (all approximately 1.4) and greater than those formed in the absence of Ni. On the other hand, the O/C ratios of the three Ni-supported oxides varied significantly from one support to another. Interestingly, Ni/CeO₂ and Ni/CeZrO_x (and not Ni/ZrO₂) define the extremes of the observed O/C ratio (**Table S4**), contrary to what might be expected from catalyst composition.

The results shown in **Figure 4** clearly indicate that chars formed in the presence of catalysts, especially in the presence of Ni-bearing catalysts, are compositionally distinct from thermal chars. Decarboxylation and dehydration reaction pathways may both be active for char formation, as shown schematically in **Figure 4**. Alternative pathways include increased aromatization during thermal HTL to account for the lower H/C ratio observed and hydrogenation to account for the greater H/C ratio observed in the presence of Ni-impregnated oxides.

Table 4. Energy recoveries of biocrude oil, aqueous-soluble product (usable for CH₄ production), gas product, and total.

Catalyst	$ER_{\text{biocrude oil}}$ (%)	$ER_{\text{RNG, estimated}}$ (%) ^a	RNG Yield (MJ/kg Food Waste)	ER_{Gas} (%) ^a	ER_{Overall} (%)
Thermal (H_2)	30.8 \pm 4.6	6.5 \pm 1.9	1.8 \pm 0.5	8.6	45.9 \pm 5.0
CeO ₂	31.2 \pm 1.7	7.5 \pm 2.1	2.0 \pm 0.6	13.5	52.2 \pm 2.7
ZrO ₂	30.3 \pm 1.6	9.1 \pm 0.3	2.5 \pm 0.1	15.6	54.9 \pm 1.7
CeZrO _x	34.0 \pm 2.6	7.8 \pm 1.8	2.1 \pm 0.5	24.5	66.3 \pm 3.1
Ni/CeO ₂	32.3 \pm 3.5	11.3 \pm 2.7	3.1 \pm 0.7	9.0	52.6 \pm 4.4
Ni/ZrO ₂	39.2 \pm 1.5	11.5 \pm 2.4	3.1 \pm 0.7	12.7	63.5 \pm 2.9
Ni/CeZrO _x	32.2 \pm 5.5	14.0 \pm 6.4	3.8 \pm 1.7	13.1	59.3 \pm 8.4

^a Estimated based on the gas composition and corresponding heating values of gas components. RNG: Renewable natural gas. Ranges represent the standard deviation estimated based on either two or three repeated tests.

Table 5. Impacts of Ni-based catalysts on the product distribution and *ER* of biocrude oil from literature.

Catalyst	Feedstock	Temperature (°C), Time (min), Gas	Product Carbon Yields (wt%, d.b.)		<i>ER</i> Improvement of Biocrude Oil ^b	Ref.
			Char	Biocrude Oil		
No catalyst	Rice straw	300, 120, N ₂	15.1 ^a	27.4		Younas et al.,2017
Ni/CeO ₂	Rice straw	300, 120, N ₂	9.9 ^a	31.6	1.15	Younas et al.,2017
No catalyst	<i>Nannochloropsis salina</i>	340, 30, N ₂	3.1 ^a	51.4 ^a		Li et al.,2014
NiMo/Al ₂ O ₃	<i>Nannochloropsis salina</i>	340, 30, H ₂	3.4 ^a	72.5 ^a	1.30 ^c	Li et al.,2014
No catalyst	Vermicompost	340, 30, N ₂	26.8 ^a	39.9		Li et al.,2014
NiMo/Al ₂ O ₃	Vermicompost	340, 30, H ₂	35.7 ^a	53.1	1.14 ^c	Li et al.,2014
No catalyst	<i>Spirulina platensis</i>	350, 60, N ₂	5.8 ^a	62.8		Jena et al.,2012
NiO	<i>Spirulina platensis</i>	350, 60, N ₂	5.7 ^a	49.0	0.82	Jena et al.,2012
No catalyst	Food waste	300, 60, N ₂	41.5±26.1	23.8±7.4		This study
Ni/CeZrO _x	Food waste	300, 60, H ₂	4.3±0.3	32.4±1.7	1.19 ^c	This study
No catalyst	Food waste	300, 60, N ₂	41.5±26.1	23.8±7.4		This study
Ni/CeO ₂	Food waste	300, 60, H ₂	10.1±2.5	35.9±3.9	1.19 ^c	This study
No catalyst	Food waste	300, 60, N ₂	41.5±26.1	23.8±7.4		This study
Ni/ZrO ₂	Food waste	300, 60, H ₂	1.3±0.2	41.8±4.1	1.44 ^c	This study

^a Mass basis. ^b *ER* Improvement is equal to the ratio of *ER* of catalytic HTL to *ER* of non-catalytic HTL. ^c The energy content of H₂ co-feed is included in *ER* of catalytic HTL. d.b.: dry basis. *ER*: energy recovery. Ranges represent the standard deviation of either two or three repeated tests.

Figure 5 provides gas component yield data. In all cases, the gases consisted mainly of carbon dioxide (CO₂), carbon monoxide (CO), hydrogen (H₂), and small amounts of methane (CH₄) and ethylene (C₂H₄). **Figure S8** shows the estimated HHV values of gas product under all experimental conditions.

CO is the product of decarbonylation,⁷¹ while CO₂ is formed either directly from decarboxylation or indirectly from CO.⁷² The presence of metal oxides increases CO₂ yields, decreases the O/C ratio of biocrude oil, and decreases CO yields. Collectively, observations that metal oxides promote decarboxylation and/or decarbonylation are consistent with previous reports.⁷³⁻⁷⁵ In fact, decarboxylation of biomass-derived bio-oils and model compounds has been studied extensively over acidic catalysts.⁷⁶ C₂H₄ may be produced either from dehydrogenation of protein-derived short acids or dehydration of carbohydrate-derived ethanol.^{77, 78} H₂ is residual from the initial charge and can be produced from dehydrogenation reactions, as has been reported under pyrolytic conditions and may be possible under HTL conditions.⁷⁹ Ni catalyzes hydrogenation in the reducing H₂ yields.⁸⁰ Interestingly, the main effect of the catalysts is to increase the CO₂ and H₂ yields and decrease the CO yield, indicating that the catalysts may be effective for promoting WGS as well.^{62, 63}

As shown in **Figure S9**, use of an oxide catalyst results in net H₂ generation, while the Ni-impregnated catalysts result in partial H₂ consumption. After separation, the resulting gas streams produced using the Ni-oxide catalysts can provide H₂ for recycle to the HTL reactor, an ethylene-rich hydrocarbon stream, and a pressurized CO₂ stream suitable for utilization or capture.^{81, 82}

The biocrude, gas phase, and aqueous phase are readily converted into energy products. The biocrude is appropriate for upgrading to renewable liquid fuel. In the gas phase, the high-pressure CO₂ is especially suitable for capture and the H₂ can be recycled to the CHTL reactor or used for upgrading the biocrude. If recycled, then the

effective ER need not account for the hydrogen co-feed, increasing the ER observed for use of Ni/ZrO₂ to 43.2%.

The aqueous phase is appropriate for RNG production, either by hydrothermal gasification⁸³ or anaerobic digestion.⁸⁴ Using aqueous TOC measurements (Table S5), the RNG potential of the aqueous phase can be estimated using literature methods.^{84, 85} Table 4 summarizes the estimated RNG yields and the corresponding metric, $ER_{RNG,estimated}$.

The ER values calculated for the biocrude, aqueous phase, and gas products can be summed into an overall metric, $ER_{overall}$, as shown in Table 4. The total ER available for Ni-supported metal oxide and metal oxide catalysts outperform that of controls by 14–44% due to the significant char reduction and transference of carbon into more usable products. Specifically, according to the life-cycle assessment model reported by Sun et al.,¹⁸ using the Ni/ZrO₂ catalyst can reduce the energy input to energy output ratio and the greenhouse gas emissions by approximately 10% compared with HTL performed without catalyst. Similarly, the minimum selling price of biocrude could be reduced by as much as 15%, based on the techno-economic analysis model performed by Ou et al.⁸⁶

Table 5 compares the performance observed for the Ni-based catalysts with some previous literature results obtained for CHTL of algae or biomass.^{68, 87, 88} Because product yields are strongly dependent on the feed, data reported for both HTL and CHTL conditions are provided

to isolate the catalyst effect. As expected, from carbon yield and HHV results, the maximum $ER_{biocrude}$ was obtained using Ni/ZrO₂, approximately 40%.

The impact of the catalyst on $ER_{biocrude}$ is shown directly in Table 5 as the ratio of the values obtained with and without catalyst. ER values from literature studies were recalculated to account for the addition of H₂ co-feed so that all ER values are calculated on the same basis. Table 5 shows that the performance of the Ni-based catalysts, especially Ni/ZrO₂, was superior to most previous literature reports in terms of simultaneous char reduction, biocrude yield improvements, and ER performance. The ER performance observed for CHTL of *Nannochloropsis salina* over Ni–Mo/Al₂O₃ is in the same range as observed in this work. However, in comparison with Ni/ZrO₂, Ni–Mo/Al₂O₃ produces about 3-times more char and the Ni–Mo/Al₂O₃ catalyst actually increases char yields relative to non-catalytic HTL conditions. Accordingly, Ni-impregnated zirconia and ceria catalysts show promise for simultaneously reducing char yield and maintaining bio-oil quality and yield.

3.3 Catalyst Stability and Reuse Tests

The previous discussion on performance suggests that the Ni-impregnated catalysts have potential for improving ER obtained from HTL processing of food waste. To be economically viable, the catalysts must also be stable under the harsh reaction conditions associated with HTL. Several deactivation methods must be considered: 1) sulfur poisoning, 2) Ni(CO)₄ formation, 3) carbon deposition, 4) mineralization or decrystallization, 5) leaching Ni of sintering of Ni particles.

The sulfur content of food waste is < 1 wt%,⁸⁹ meaning that sulfur poisoning should not be a major deactivation mechanism. Consistent with this expectation, sulfides were never observed in the used catalysts. Conditions that favor Ni(CO)₄ formation – i.e., temperature < 230 °C and high CO partial pressure – were avoided, meaning that this deactivation route should be negligible.³⁸ Limiting carbon deposition was a major emphasis of this work, and the char reduction observed after Ni impregnation suggests that it is an effective method for minimizing carbon deposition.

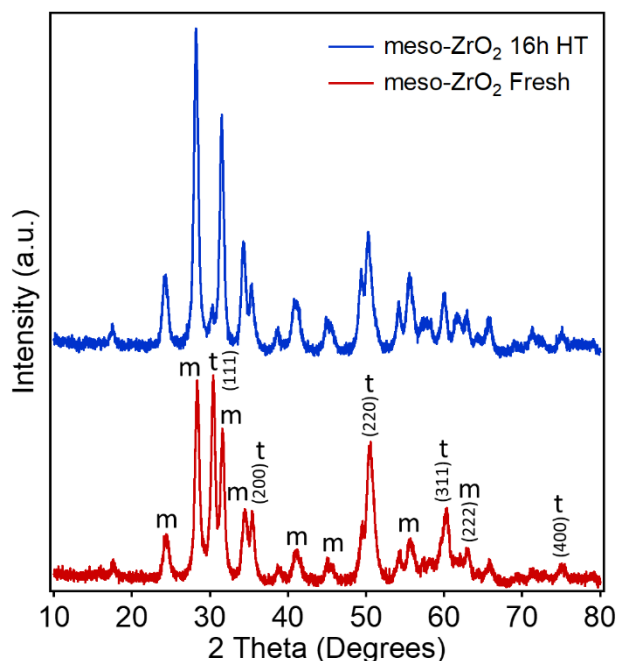


Figure 6. XRD patterns of fresh ZrO₂ and the used ZrO₂ under 300 °C and 16 hours. t: tetragonal. m: monoclinic. HT: hydrothermal treatment.

Table 6. CHTL product yields of fresh and used Ni/ZrO₂ catalysts.

Catalyst	Carbon Yield (wt%)			
	Biocrude Oil	Char	Aqueous Phase	Gas
Ni/ZrO ₂	41.8±4.1	1.3±0.2	31.1±6.9	11.4±0.0
Used Ni/ZrO ₂ ^a	41.6±2.8	2.7±1.8	29.9±9.2	11.5±2.0

^a Used Ni/ZrO₂ represents the regenerated catalyst obtained through decoking and reducing the spent Ni/ZrO₂ catalyst after CHTL.

This leaves the most likely de-activation mechanisms as mineralization and decrystallization or Ni sintering and leaching.⁹⁰ Accordingly, catalyst stability to mineralization, leaching, and sintering was evaluated after hydrothermal endurance tests (16 h), after a single use, and – for the most effective catalyst – by recovery and reuse.

Hydrothermal endurance tests were performed by placing the catalyst in liquid water at 300 °C for 16 h. The purpose of hydrothermal endurance tests was to evaluate crystalline stability at time scales appropriate for kinetically limited degradation phenomena,⁹⁰ without interference from organic reactants, and without requiring removal of carbon deposits prior to characterization. The crystalline structures of fresh and used catalysts were investigated using X-ray diffraction (XRD).

Figure 6 shows XRD diffractograms obtained for ZrO₂ before and after the hydrothermal endurance test. The water treatment decreased the intensities of the peaks associated with the ZrO₂ tetragonal phase, at 30.2°, 35.4°, 50.4°, and 60.2° (JCPDS-ICDD #50-1089). However, the XRD pattern confirms that the polycrystalline structure was maintained, and the more thermodynamically stable monoclinic phase (JCPDS-ICDD #37-1484) was still present in the ZrO₂ after the 16-hour hydrothermal stability test. These observations are consistent with the high hydrothermal stability of ZrO₂.⁹¹

Figure S1 shows similar data for Ni/CeO₂ and Ni/CeZrO_x and indicates that the crystal structures of Ni/CeO₂ and Ni/CeZrO_x were nearly unchanged after hydrothermal reaction. Interestingly, evidence of CeCO₃OH formation (JCPDS-ICDD #41-0013) was detected in the XRD patterns of both Ni/CeO₂ and Ni/CeZrO_x, suggesting a potential change in oxidation state during water exposure and consistent with previous studies on the interaction between water and CeO₂.⁹²

Similarly, nickel particle sizes were estimated from XRD diffractograms using the Scherrer equation before and after the hydrothermal endurance test. **Table S1** shows that the Ni particle size decreased slightly for all three Ni-impregnated catalysts after the hydrothermal endurance tests, suggesting that leaching of trace amount of Ni occurred under hydrothermal conditions, which was in agreement with the observation in previous studies.^{93, 94}

To evaluate further, the aqueous phase obtained from a representative catalytic test was analyzed for metal content using ICP-MS. The nickel loading and the nickel percent leached into the CHTL aqueous phase of the Ni/ZrO₂ obtained after the 2nd-cycle were 7.74 wt% (as compared to 8.24 wt% Ni content in the fresh catalyst) and 0.06 wt% (on a basis of Ni amount in fresh catalyst),

respectively, indicating that Ni leaching should be considered a minor catalyst deactivation route.

The hydrothermal endurance test permits characterization on relevant time scales (16 h) and without interference from organic reactants. To complement the hydrothermal endurance test, used catalysts were recovered, calcined in air to remove char, and characterized using XRD and Raman spectroscopy. The Raman spectra (**Figures S5-S7**) of used CeO₂, Ni/CeO₂, CeZrO_x, and Ni/CeZrO_x catalysts display all of the same features as the original materials, but with more intense bands. The increased intensity is consistent with removal of surface defects (e.g. oxygen vacancies) during use and/or regeneration. The XRD patterns and Raman spectra (**Figures 6, S1, and S6**) obtained for ZrO₂ and Ni/ZrO₂ before use and after regeneration indicate a transition from primarily monoclinic phase to a tetragonal phase.⁹⁵ The zirconia catalyst remains in the monoclinic state after exposure to hydrothermal conditions, indicating that the transition to the tetragonal phase occurred during thermal regeneration at 550 °C. Decreasing the regeneration temperature from that used here (550 °C) should eliminate this problem.

To evaluate the reusability of the best catalyst, Ni/ZrO₂, a sample was recovered after its use, regenerated by calcining in air, and used for a second cycle. **Table 6** indicates negligible differences between the biocrude and char yields obtained in the first and second uses. Likewise, the XRD diffractogram (**Figure S1**) of the catalyst recovered after its second use was nearly identical to that corresponding to the first use, indicating negligible loss of structure. Accordingly, all of these considerations are consistent with stable catalytic activity under HTL conditions, encouraging continued evaluation.

3.4 Molecular-Level Characterization of the Biocrude

Lastly, the molecular composition of the biocrude was analyzed in detail using a series of complementary methods, with the objective being to gain insight in the HTL and CHTL mechanisms. Accordingly, biocrude chemical composition was investigated at the molecular level using GC-MS, GC×GC, (+) APPI FT-ICR MS, and ¹H NMR.

Beginning with GC-MS, the full-scan total ion chromatograms (TIC) were dominated by fatty acid amides (C14-C18) (**Figure S10 and Table S6**). This is reasonable as fatty acid amides are formed by reaction of fatty acids with amines, and amines are the natural product of protein hydrolysis.⁹⁶ The presence of fatty acid amides in the biocrude gives a clear target for hydrodenitrogenation.^{97, 98}

Interestingly, unlike the other biocrudes, GC-MS indicates that the ZrO₂ and especially Ni/ZrO₂ biocrude contained fatty acid ester peaks (e.g. 63.8 min: ethyl hexadecanoate, and 70.2 min: ethyl octadecanoate, etc.). The fatty acid

ester content of the ZrO₂ biocrude determined from GC-MS analysis is consistent with its bulk properties, including especially its C-H-O composition and greater HHV value compared with the other biocrude products (**Table 3**). Formation of fatty acid esters indicates that the ZrO₂ catalysts possess esterification activity, similar to previous reports on bio-diesel catalysis.⁹⁹

To extract further information from the biocrude obtained using the best catalyst (Ni/ZrO₂), this sample was analyzed using comprehensive two-dimensional GC high-resolution time-of-flight mass spectral detector (GC×GC-HRT). Compared to single dimension GC-MS (unit resolution), GC×GC-HRT has greater resolving power and provides much more detailed chemical information on complex samples.¹⁰⁰ Interestingly, and in contrast with GC-MS, GC×GC-HRT indicated that the fatty acid content was greater than the corresponding fatty acid amide content, with the amide-to-fatty acid ratio varying from 5:1 to 10:1 (**Figure S11**). The discrepancy between GC-MS and GC×GC-HRT can be attributed to co-elution in the former and the greater mass resolution of the latter. Future work on biocrude analysis should prioritize GC×GC-HRT over GC-MS.

To understand lipid content in greater details, GC×GC analysis was performed on a derivatized sample of lipids extracted from the feed and compared with analysis of biocrudes obtained using HTL and CHTL with Ni/ZrO₂ as the catalyst (**Figure S12**). In all cases, C16 fatty acids are more abundant than C12, C14, and C18 varieties. Interestingly, the C18 fatty acid is not apparent in the HTL or CHTL biocrude, suggesting that it is more reactive than other fatty acids.¹⁰¹ This is a new finding under HTL conditions, but a similar effect of chain length on fatty acid reactivity has been reported for thermal aging of bio-diesel.¹⁰² Increasing reactivity with increasing chain length suggests the importance of H-abstraction in the mechanism, since H-abstraction rates are proportional to the number of abstractable H atoms present on a molecule.¹⁰³ Similarly, the C12, C14, and C16 fatty acids are present in saturated forms, while the C18 fatty acid is present both in saturated and monounsaturated form. The unsaturated C18 is expected to be more reactive than the saturated form, as the double bond provides opportunities for mid-chain hydrolysis and/or radical formation reactions.

GC and GC×GC analysis provide detailed molecular information for compounds that evaporate at temperatures less than 300 °C, but little or no information on the less volatile and/or thermally unstable components of the biocrude. Accordingly, biocrude was analyzed using ¹H NMR spectroscopy and FT-ICR MS.^{52, 101} ¹H NMR and FT-ICR MS do not provide as much structural detail as can be determined from GC and especially GC×GC-MS analysis; however, neither technique is limited to sample volatility.

Accordingly, ¹H NMR and FT-ICR MS ideally complement analysis using GC and GC×GC.

Figure S13 shows that the most prominent peaks in the ¹H NMR spectra are located at 0.81–88 ppm and 1.18–1.26 ppm, indicating the abundance of aliphatic methyl protons and methylene protons in alkyl chains, respectively, in all biocrudes regardless of the catalysts used. A third major peak, located at 2.09–2.18 ppm, represents aliphatic protons in the α-position relative to a heteroatom in straight/branched amides or carboxylic acids. A minor peak, appearing at 5.31–5.38 ppm, corresponds to non-conjugated olefinic protons, consistent with unsaturated lipids. No peak appears at 9.0–10.1 ppm, suggesting negligible aldehyde content in the biocrude. This is consistent with the high reactivity of aldehyde,¹² resulting in its complete consumption under these reaction conditions.

To gain further information into heteroatom content, the peak area ratios of 2.09–2.18 ppm (protons adjacent to heteroatoms) to 1.18–1.26 ppm (methylene protons) were estimated for all biocrudes. ZrO₂ and Ni/ZrO₂ biocrudes have smaller peak area ratios than the rest of biocrudes (**Table S7**), indicating that ZrO₂ and Ni/ZrO₂ biocrudes have the greatest methylene content and least fatty amide content compared with the biocrudes obtained using the other catalysts, which is consistent with the GC results.

The biocrude was further analyzed by (+) APPI FT-ICR MS. The resolving power and mass accuracy (50–250 ppb) of FT-ICR MS allow for elemental composition assignment to the tens of thousands of mass spectral peaks detected in each sample. As with GC and NMR analysis, fatty amides, distinguished by their molecular formulas of the form C₁₆₋₂₂H₃₅₋₄₂N₁O₁, were a major component identified using FT-ICR MS. In addition to the N₁O₁ class, the most abundant heteroatom classes identified in the biocrude correspond to N₁O₂, N₂O₂, N₁O₃, N₂O₃, and N₂O₁ multicyclic compounds (~C₁₄–C₂₅ with double bond equivalents between 4–13) likely comprised of hydroxyl, aldehyde, and ketone groups (**Figures S14 and S15**). Potential structures corresponding to these classes include pyrrolidinediones, pyrimidinediones, quinoxalines, indoles, and phenazines, respectively.^{104, 105} Interestingly, the types of compounds present in the biocrudes did not depend strongly on the catalyst.

Additionally, **Figure S16** shows that the molecular weight distributions (MWD) of biocrude obtained using different catalysts fall in the range from 150 and 1000 Da, with a mean molecular weight of approximately 310 Da and again independent of catalyst. In summary, these advanced methods shed light on the comprehensive molecular-level chemistry of biocrudes, previously unattainable with traditional analytical platforms, and reveal a complex

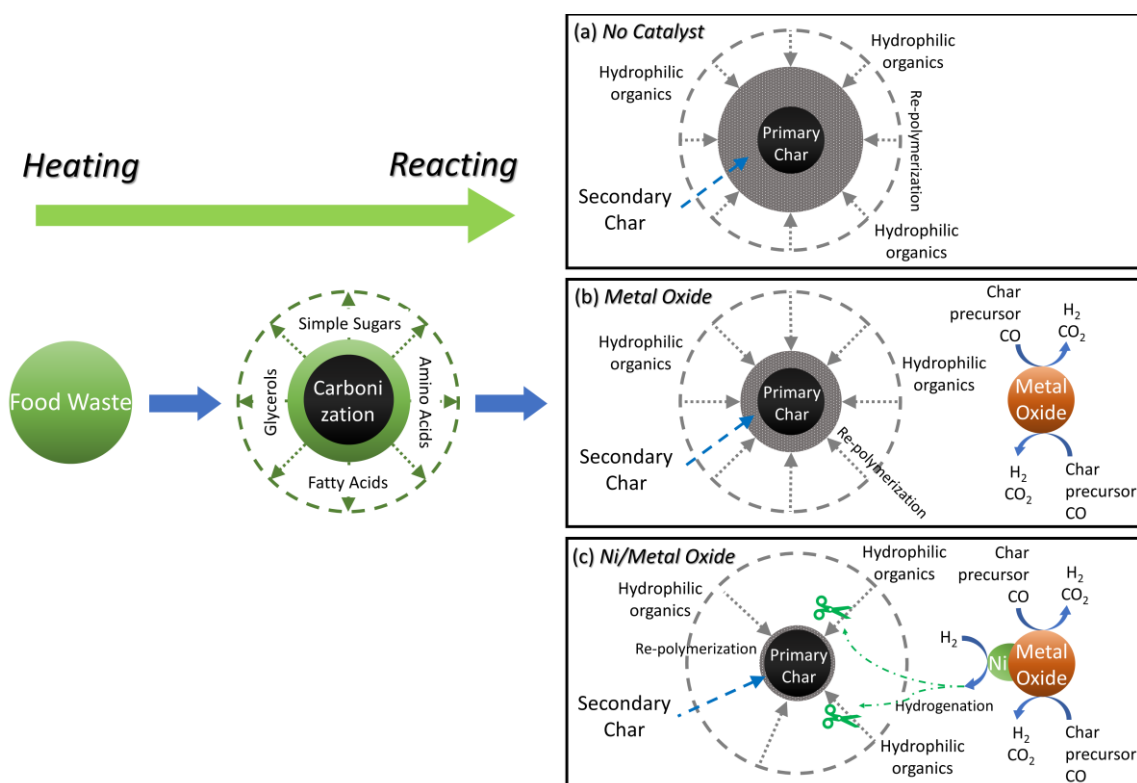


Figure 7. The schematic diagram of plausible char reduction mechanism in the CHTL using the metal oxide and nickel-supported metal oxide catalysts.

continuum of biocrude oils before and after the use of Ni-impregnated heterogeneous catalyst.

The molecular-level analysis of the biocrude can be combined with the char and gas composition analysis to support a plausible mechanism of catalytic control of char formation, as shown in **Figure 7**. In general, char may be formed from primary and secondary mechanisms.¹⁰⁶ Food waste is fed to the reactor as insoluble particles (20–60 μm). During heat-up, water cannot access organic compounds trapped within the particle. As the organic compounds contained within the particle thermally decompose, the fragments cannot be removed rapidly and instead carbonize to form primary char.¹⁰⁶ The organic components in the outer shell of the food waste particles are depolymerized and released into the liquid phase.^{101, 107, 108} In the absence of catalyst, some of the highly reactive water-soluble products re-polymerize to form biocrude or secondary char with less H and O content than primary char.¹⁰⁹

In the presence of metal oxides, most secondary char precursors deposited on the catalyst surface must be removed and reacted via oxidation reactions on the catalyst rather than accumulating as char (**Figure 7**). Specifically, the metal oxides appear to reduce the tendency of reactive oxygenates to form char, resulting in the char with less oxygen content than observed in the absence of catalyst (**Figure 7b**). Ni has the additional effect of hydrogenating char precursors, thereby increasing the

H content of the char while also inhibiting char formation and decreasing the hydrogen yield (**Figure 7c**).

The importance of the WGSR is supported by the observation that CO yield decreases in the presence of oxide catalysts in parallel with increasing H₂ and CO₂ yields. Both CeO₂ and CeZrO_x exhibit redox properties and are capable of catalyzing the low-temperature WGSR.^{110, 111} Redox reactions imply a change in Ce oxidation state. In fact, the aforementioned appearance of a band attributable to CeCO₃OH (JCPDS-ICDD #41-0013) observed in XRD analysis of used Ce-containing catalysts indicates transition between Ce⁴⁺ and Ce³⁺ (**Figure S1**).

Unlike Ce, Zr is not widely reported as a redox active material,¹¹² and hydrothermal exposure of ZrO₂ does not give rise to bands attributable to Zr³⁺ (**Figure S1**). ZrO₂ must therefore inhibit char formation by a different mechanism from CeO₂ and CeZrO_x, which should be studied in future research. Transesterification to form fatty acid esters and remove reactive groups from the mixture prior to forming char is a likely pathway, given the effectiveness of ZrO₂-based catalysts for promoting esterification reactions and thereby increasing biocrude yields.

In the presence of Ni-impregnated metal oxides, Ni further reduces char yields, increases yields of water-soluble carbon, and results in H₂ consumption relative to that observed for the metal oxides on their own. Formation of

secondary char may be further inhibited by preventing char growth on the catalyst surface as well as limiting aqueous condensation via hydrogenation reactions (Figure 7). This mechanism is consistent with the H/C and O/C ratios obtained for the hydrogen-rich char formed in the presence of Ni-impregnated catalysts (Figure 4). This mechanism can be confirmed by further characterization of the HTL aqueous phase formed in the presence and absence of catalysts.

Conclusions

Three metal oxide supported Ni catalysts, Ni/CeZrO_x, Ni/ZrO₂, and Ni/CeO₂, were investigated for CHTL of food waste to reduce char yield and improve energy recovery as useful products. The Ni-based catalysts decreased char yield significantly from 16–24% to 1–10% (carbon basis). Ni/ZrO₂ was the most effective catalyst tested for reducing char yield and simultaneously produced the greatest yield of biocrude with the greatest HHV (39.3 MJ kg⁻¹) and greatest ER as biocrude (39.2%). After accounting for the energy content that could be recovered from the gas product and aqueous phase, the net effect was to increase the ER as usable products from 45.9 ± 5.0% without catalyst to 63.5 ± 2.9% with Ni/ZrO₂.

All three catalysts were hydrothermally stable, with minor decreases in Ni particle size observed after 16 h of exposure to HTL conditions. The thermal stability of Ni/CeZrO_x and Ni/CeO₂ was greater than that of Ni/ZrO₂ as the crystalline structure of Ni/ZrO₂ transformed from tetragonal to monoclinic during regeneration. Tests with reused Ni/ZrO₂ indicate negligible decrease in biocrude yield or increase in char yield after two cycles, with 93% nickel retention.

The biocrude was analyzed using several complementary methods. Fatty acids and fatty amides were present in all samples. Heavy compounds present in the samples were likely pyrrolidinediones, quinolines, pyrimidinediones, quinoxalines, indoles, and phenazines. Esterification reactions to remove reactive precursors and WGS were suggested as plausible pathways responsible for char reduction in the presence of the catalysts used here.

Conflicts of interest

There are no conflicts to declare.

Acknowledgements

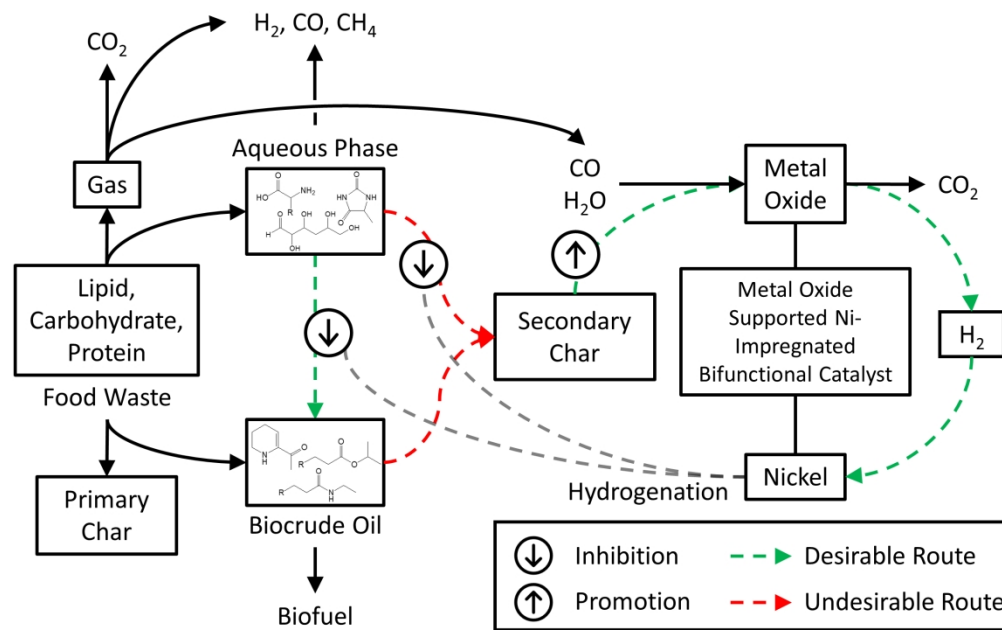
This work was funded by a Phase II DOE SBIR contract (DE-SC0015784), the DOE Bioenergy Technology Office (DE-EE0008513), and the MassCEC. The authors thank: Alex Maag, Department of Biological and Environmental Engineering at Cornell University, for training several of the authors; Wenwen Yao, Department of Environmental Science at WPI, for TOC and ICP analysis; Mainstream Engineering for the characterization of the oil and solids samples; and Azadeh Zaker, Department of Chemical Engineering in WPI, for gas composition analysis. A portion of this work was performed at the National High Magnetic Field Laboratory Ion Cyclotron Resonance user facility, which is supported by the NSF Division of Materials Research and Division of Chemistry through DMR 16-44779 and the State of Florida. Authors DVFA and CIR performed this work as part of their Major Qualifying Project, a degree requirement of Worcester Polytechnic Institute.

Notes and references

1. USEPA, Sources of Greenhouse Gas Emissions, <https://www.epa.gov/ghgemissions/sources-greenhouse-gas-emissions>, (accessed 08/23, 2019).
2. USEIA, Biomass—Renewable Energy from Plants and Animals, https://www.eia.gov/energyexplained/?page=biomass_home, (accessed 08/23, 2019).
3. M. Langholtz, B. Stokes and L. Eaton, *Oak Ridge National Laboratory, Oak Ridge, Tennessee, managed by UT-Battelle, LLC for the US Department of Energy*, 2016, **2016**, 1-411.
4. J. Shen, C. Zhao, G. Liu and C. Chen, *Waste and biomass valorization*, 2017, **8**, 1119-1126.
5. USEPA, Municipal Solid Waste Generation, Recycling, and Disposal in the United States Tables and Figures for 2015, <http://www.epa.gov/osw/nonhaz/municipal/msw99.htm>, (accessed 06/21, 2019).
6. EERE, *Biofuels and Bioproducts from Wet and Gaseous Waste Streams: Challenges and Opportunities*, Bioenergy Technologies Office, U.S. DOE, 2017.
7. B. F. Staley and M. A. Barlaz, *Journal of Environmental Engineering*, 2009, **135**, 901-909.
8. E. A. Scano, C. Asquer, A. Pistis, L. Ortu, V. Demontis and D. Cocco, *Energy Conversion and Management*, 2014, **77**, 22-30.
9. A. Badgett, E. Newes and A. Milbrandt, *Energy*, 2019, **176**, 224-234.
10. P. S. Murthy and M. M. Naidu, *World Applied Sciences Journal*, 2010, **8**, 199-205.
11. Z. Sun, M. Li, Q. Qi, C. Gao and C. S. K. Lin, *Applied biochemistry and biotechnology*, 2014, **174**, 1822-1833.
12. A. Maag, A. Paulsen, T. Amundsen, P. Yelvington, G. Tompsett and M. Timko, *Energies*, 2018, **11**, 564.

13. M. Deniel, G. Haarlemmer, A. Roubaud, E. Weiss-Hortala and J. Fages, *Renewable and Sustainable Energy Reviews*, 2016, **54**, 1632-1652.
14. D. R. Vardon, B. K. Sharma, G. V. Blazina, K. Rajagopalan and T. J. Strathmann, *Bioresource Technology*, 2012, **109**, 178-187.
15. S. S. Toor, L. Rosendahl and A. Rudolf, *Energy*, 2011, **36**, 2328-2342.
16. J. A. Ramirez and T. J. Rainey, *Journal of Cleaner Production*, 2019, **229**, 513-527.
17. Y. Tao and F. You, in *Computer Aided Chemical Engineering*, Elsevier, 2019, vol. 46, pp. 1705-1710.
18. C.-H. Sun, Q. Fu, Q. Liao, A. Xia, Y. Huang, X. Zhu, A. Reungsang and H.-X. Chang, *Energy*, 2019, **171**, 1033-1045.
19. A. Ahamed, K. Yin, B. J. H. Ng, F. Ren, V.-C. Chang and J.-Y. Wang, *Journal of Cleaner Production*, 2016, **131**, 607-614.
20. A. A. Peterson, F. Vogel, R. P. Lachance, M. Fröling, M. J. Antal Jr and J. W. Tester, *Energy & Environmental Science*, 2008, **1**, 32-65.
21. C. Zhang, X. Tang, L. Sheng and X. Yang, *Green Chemistry*, 2016, **18**, 2542-2553.
22. C. He, A. Giannis and J.-Y. Wang, *Applied Energy*, 2013, **111**, 257-266.
23. F. Cheng, K. Mallick, S. M. H. Gedara, J. M. Jarvis, T. Schaub, U. Jena, N. Nirmalakhandan and C. E. J. B. t. Brewer, 2019, **292**, 121884.
24. K. Wiedner, C. Naisse, C. Rumpel, A. Pozzi, P. Wiczorek and B. Glaser, *Organic Geochemistry*, 2013, **54**, 91-100.
25. Z. Liu, F.-S. Zhang and J. Wu, *Fuel*, 2010, **89**, 510-514.
26. B. de Caprariis, I. Bavasso, M. P. Bracciale, M. Damizia, P. De Filippis and M. Scarsella, *Journal of Analytical and Applied Pyrolysis*, 2019, **139**, 123-130.
27. S. Koley, M. S. Khadase, T. Mathimani, H. Raheman and N. Mallick, *J Energy Conversion and Management*, 2018, **163**, 111-121.
28. E. Furimsky and F. E. Massoth, *Catalysis Today*, 1999, **52**, 381-495.
29. C. Wang, Y. Fan, U. Hornung, W. Zhu and N. Dahmen, *Journal of Cleaner Production*, 2019, 118586.
30. A. Ross, P. Biller, M. Kubacki, H. Li, A. Lea-Langton and J. Jones, *Fuel*, 2010, **89**, 2234-2243.
31. S. Zou, Y. Wu, M. Yang, K. Imdad, C. Li and T. Junmao, *Energy* 2010, **35**, 5406-5411.
32. C. Liu, L. Kong, Y. Wang and L. Dai, *Algal research*, 2018, **33**, 156-164.
33. B. Meryemoğlu, A. Hasanoğlu, S. Irmak and O. Erbatur, *Bioresource technology*, 2014, **151**, 278-283.
34. J. Yin, Z. Cheng, L. Guo, S. Li and H. Jin, *International Journal of Hydrogen Energy*, 2017, **42**, 4642-4650.
35. J. Zhang, M. Wang, S. Xu and Y. Feng, *Fuel Processing Technology*, 2019, **192**, 147-153.
36. Y. Liu, S. Wang, T. Sun, D. Gao, C. Zhang and S. Wang, *Applied Catalysis B: Environmental*, 2012, **119**, 321-328.
37. A. G. Gayubo, A. Alonso, B. Valle, A. T. Aguayo, M. Olazar and J. Bilbao, *Fuel*, 2010, **89**, 3365-3372.
38. D. Miksa and T. B. Brill, *Industrial & engineering chemistry research*, 2001, **40**, 3098-3103.
39. Z. Huang, Z. Deng, F. He, D. Chen, G. Wei, K. Zhao, A. Zheng, Z. Zhao and H. Li, *International Journal of Hydrogen Energy*, 2017, **42**, 14458-14470.
40. J. Jones, H. Xiong, A. T. DeLaRiva, E. J. Peterson, H. Pham, S. R. Challa, G. Qi, S. Oh, M. H. Wiebenga and X. I. P. Hernández, *Science*, 2016, **353**, 150-154.
41. S. Roy and J. Ghose, *Materials research bulletin*, 2000, **35**, 1195-1203.
42. D. J. Zastrow and P. A. Jennings, presented in part at the AIChE annual meeting, San Francisco, CA, 2013.
43. USDA-ARS, *Journal*, 2018.
44. D. C. Elliott, P. Biller, A. B. Ross, A. J. Schmidt and S. B. Jones, *Bioresource technology*, 2015, **178**, 147-156.
45. X. Liao, Y. Zhang, M. Hill, X. Xia, Y. Zhao and Z. Jiang, *Applied Catalysis A: General*, 2014, **488**, 256-264.
46. P. Käßner and M. Baerns, *Applied Catalysis A: General*, 1996, **139**, 107-129.
47. E. Rodrigues, T. Keller, S. Mitchell and J. Pérez-Ramírez, *Green Chemistry*, 2014, **16**, 4870-4874.
48. F. Cheng, G. A. Tompsett, C. M. Murphy, A. R. Maag, N. Carabillo, M. Bailey, J. J. Hemingway, C. I. Romo, A. D. Paulsen, P. E. Yelvington and M. T. Timko, *ACS Sustainable Chem. Eng.*, 2020, **8**, 6877-6886.
49. J. Akhtar and N. A. S. Amin, *Renewable and Sustainable Energy Reviews*, 2011, **15**, 1615-1624.
50. W. Wagner and A. Pruß, *J Phys Chem Ref Data* 2002, **31**, 387-535.
51. A. Demirbaş, *Fuel*, 1997, **76**, 431-434.
52. A. M. McKenna, R. K. Nelson, C. M. Reddy, J. J. Savory, N. K. Kaiser, J. E. Fitzsimmons, A. G. Marshall and R. P. Rodgers, *Environmental science & technology*, 2013, **47**, 7530-7539.
53. N. K. Kaiser, J. P. Quinn, G. T. Blakney, C. L. Hendrickson and A. G. Marshall, *Journal of the American Society for Mass Spectrometry*, 2011, **22**, 1343-1351.
54. A. Larimi and S. Alavi, *Fuel*, 2012, **102**, 366-371.
55. L. Xu, H. Song and L. Chou, *International journal of hydrogen energy*, 2012, **37**, 18001-18020.
56. R. Milo and R. Phillips, How Big Are Biochemical Nuts and Bolts?, <http://book.bionumbers.org/how-big-are-biochemical-nuts-and-bolts/>, (accessed April 10, 2020, 2020).
57. V. Doubrovsky, I. Y. Yanina and V. Tuchin, Saratov, Russian, 2011.
58. B. Peng, C. Zhao, S. Kasakov, S. Foraita and J. A. Lercher, *Chemistry—A European Journal*, 2013, **19**, 4732-4741.
59. J. Wang, Z. Li, S. Zhang, S. Yan, B. Cao, Z. Wang and Y. Fu, *Sens. Actuators B Chem*, 2018, **255**, 862-870.
60. V. A. Sadykov, M. N. Simonov, N. V. Mezentseva, S. N. Pavlova, Y. E. Fedorova, A. S. Bobin, Y. N. Bepalko, A. V. Ishchenko, T. A. Krieger and T. S. Glazneva, *Open Chem*, 2016, **14**, 363-376.
61. Q. Cai, J. Zhang, X. Chen, Z. Chen, W. Wang, G. Mo, Z. Wu, L. Zhang and W. Pan, *Journal of Physics: Condensed Matter*, 2008, **20**, 115205.
62. N. Schreiter, J. Kirchner and S. Kureti, *Catalysis Communications*, 2020, 105988.
63. M. Nizio, A. Albarazi, S. Cavadias, J. Amouroux, M. E. Galvez and P. Da Costa, *International Journal of Hydrogen Energy*, 2016, **41**, 11584-11592.
64. H. Shafaghat, Y. F. Tsang, J.-K. Jeon, J. M. Kim, Y. Kim, S. Kim and Y.-K. Park, *Chemical Engineering Journal*, 2020, **382**, 122912.
65. S. Cheng, L. Wei, M. Alsowij, F. Corbin, E. Boakye, Z. Gu and D. Raynie, *AIMS Environ Sci*, 2017, **4**, 417-430.
66. S. Kim, R. W. Kramer and P. G. Hatcher, *Analytical chemistry*, 2003, **75**, 5336-5344.
67. W. Shi, S. Li, H. Jin, Y. Zhao and W. Yu, *Energy Sources, Part A: Recovery, Utilization, and Environmental Effects*, 2013, **35**, 2149-2155.
68. U. Jena, K. Das and J. Kastner, *Applied Energy*, 2012, **98**, 368-375.

69. Z. Morvay and D. Gvozdenac, *Applied Industrial Energy and Environmental Management. Part Iii: Fundamentals for Analysis*, Wiley-IEEE Press, Hoboken, New Jersey, USA, 2008.
70. D. Hansdah, S. Murugan and L. J. A. E. J. Das, 2013, **52**, 267-276.
71. Z. Zhu, S. S. Toor, L. Rosendahl, D. Yu and G. Chen, *Energy*, 2015, **80**, 284-292.
72. G. Yu, Y. Zhang, L. Schideman, T. Funk and Z. Wang, *Energy & Environmental Science*, 2011, **4**, 4587-4595.
73. S. M. Schimming, O. D. LaMont, M. König, A. K. Rogers, A. D. D'Amico, M. M. Yung and C. Sievers, *ChemSusChem*, 2015, **8**, 2073-2083.
74. B. Kitiyanana, C. Ung-jindaa, V. Meeyoob, T. Rirksomboona and P. Rangsunvigita, 2008.
75. T. Aysu, M. M. Maroto-Valer and A. Sanna, *Bioresource Technology*, 2016, **208**, 140-148.
76. Y. Uemura, N. T. Tran, S. R. Naqvi and N. Nishiyama, 2017.
77. M. Godinho, R. d. F. Gonçalves, E. R. Leite, C. W. Raubach, N. L. Carreño, L. F. Probst, E. Longo and H. V. Fajardo, *Journal of materials science*, 2010, **45**, 593-598.
78. D. Klingler, J. Berg and H. Vogel, *The Journal of Supercritical Fluids*, 2007, **43**, 112-119.
79. J. Alvarez, S. Kumagai, C. Wu, T. Yoshioka, J. Bilbao, M. Olazar and P. T. Williams, *International Journal of Hydrogen Energy*, 2014, **39**, 10883-10891.
80. Y. Xu, J. Long, Q. Liu, Y. Li, C. Wang, Q. Zhang, W. Lv, X. Zhang, S. Qiu and T. Wang, *Energy Conversion and Management*, 2015, **89**, 188-196.
81. Z. R. Herm, R. Krishna and J. R. Long, *Microporous and Mesoporous Materials*, 2012, **151**, 481-487.
82. J. V. Lamb, J.-C. Buffet, Z. R. Turner and D. O'Hare, *Macromolecules*, 2020.
83. M. H. Waldner and F. Vogel, *Industrial & engineering chemistry research*, 2005, **44**, 4543-4551.
84. G. Tommaso, W.-T. Chen, P. Li, L. Schideman and Y. Zhang, *Bioresource technology*, 2015, **178**, 139-146.
85. R. E. Speece, *Anaerobic Biotechnology for Industrial Wastewaters*, Archae Press, Nashville, TN, 1996.
86. L. Ou, R. Thilakarathne, R. C. Brown and M. M. Wright, *Biomass and Bioenergy*, 2015, **72**, 45-54.
87. R. Younas, S. Hao, L. Zhang and S. Zhang, *Renewable Energy*, 2017, **113**, 532-545.
88. H. Li, J. Hu, Z. Zhang, H. Wang, F. Ping, C. Zheng, H. Zhang and Q. He, *Bioresource technology*, 2014, **163**, 143-151.
89. N. Ramzan, A. Ashraf, S. Naveed and A. Malik, *Biomass and bioenergy*, 2011, **35**, 3962-3969.
90. A. R. Maag, G. A. Tompsett, J. Tam, C. A. Ang, G. Azimi, A. D. Carl, X. Huang, L. J. Smith, R. L. Grimm and J. Q. Bond, *Physical Chemistry Chemical Physics*, 2019, **21**, 17880-17892.
91. C. Liu, S. Lee, D. Su, B. Lee, S. Lee, R. E. Winans, C. Yin, S. Vajda, L. Pfefferle and G. L. Haller, *Langmuir*, 2012, **28**, 17159-17167.
92. D.-W. Jeong, H.-S. Na, J.-O. Shim, W.-J. Jang and H.-S. Roh, *Catalysis Science & Technology*, 2015, **5**, 3706-3713.
93. J. A. Onwudili, A. R. Lea-Langton, A. B. Ross and P. T. Williams, *Bioresource technology*, 2013, **127**, 72-80.
94. K. Fabičovicová, O. Malter, M. Lucas and P. Claus, *Green Chemistry*, 2014, **16**, 3580-3588.
95. S. N. Basahel, T. T. Ali, M. Mokhtar and K. Narasimharao, *Nanoscale research letters*, 2015, **10**, 73.
96. Y. Fan, U. Hornung, K. Raffelt and N. Dahmen, *Journal of Analytical and Applied Pyrolysis*, 2020, 104798.
97. G. Bauserman, C. Spengler and A. Cohn, 1980.
98. N. Zhang, R. Yang, D. Zhang-Negrerie, Y. Du and K. Zhao, *The Journal of organic chemistry*, 2013, **78**, 8705-8711.
99. D. E. Lopez, J. G. Goodwin Jr, D. A. Bruce and S. Furuta, *Applied Catalysis A: General*, 2008, **339**, 76-83.
100. R. K. Nelson, C. Aeppli, J. S. Arey, H. Chen, A. H. de Oliveira, C. Eiserbeck, G. S. Fryinger, R. B. Gaines, K. Grice and J. Gros, in *Standard Handbook Oil Spill Environmental Forensics*, Elsevier, 2016, pp. 399-448.
101. F. Cheng, Z. Cui, L. Chen, J. Jarvis, N. Paz, T. Schaub, N. Nirmalakhandan and C. E. Brewer, *Applied Energy*, 2017, **206**, 278-292.
102. R. Lin, Y. Zhu and L. L. Tavlarides, *Fuel*, 2013, **106**, 593-604.
103. R. Vinu and L. J. Broadbelt, *Annual review of chemical and biomolecular engineering*, 2012, **3**, 29-54.
104. N. Sudasinghe, B. Dungan, P. Lammers, K. Albrecht, D. Elliott, R. Hallen and T. Schaub, *Fuel*, 2014, **119**, 47-56.
105. J. M. Jarvis, J. M. Billing, R. T. Hallen, A. J. Schmidt and T. M. Schaub, *Energy & Fuels*, 2017, **31**, 2896-2906.
106. T. Karayıldırım, A. Sinağ and A. Kruse, *Chemical Engineering & Technology: Industrial Chemistry - Plant Equipment - Process Engineering - Biotechnology*, 2008, **31**, 1561-1568.
107. G. Teri, L. Luo and P. E. Savage, *Energy & fuels*, 2014, **28**, 7501-7509.
108. M. Sasaki, B. Kabyemela, R. Malaluan, S. Hirose, N. Takeda, T. Adschiri and K. Arai, *The Journal of Supercritical Fluids*, 1998, **13**, 261-268.
109. C. Peng, Y. Zhai, Y. Zhu, T. Wang, B. Xu, T. Wang, C. Li and G. Zeng, *Journal of Cleaner Production*, 2017, **166**, 114-123.
110. S. Hilaire, X. Wang, T. Luo, R. Gorte and J. Wagner, *Appl Catal A*, 2004, **258**, 271-276.
111. V. Idakiev, T. Tabakova, A. Naydenov, Z.-Y. Yuan and B.-L. Su, *Applied Catalysis B: Environmental*, 2006, **63**, 178-186.
112. A. Ruiz Puigdollers, S. Tosoni and G. Pacchioni, *The Journal of Physical Chemistry C*, 2016, **120**, 15329-15337.



209x129mm (300 x 300 DPI)